Improved backward smoothing square root cubature Kalman filtering and fractional order-battery equivalent modeling for adaptive state of charge estimation of lithium-ion batteries in electric vehicles.

ZHOU, J., WANG, S., CAO, W., XIE, Y. and FERNANDEZ, C.

2023

Improved Backward Smoothing Square Root Cubature Kalman Filtering and Fractional Order-Battery Equivalent Modeling for Adaptive State of Charge Estimation of Lithium-Ion Batteries in Electric Vehicles

Jiani Zhou[1], Shunli Wang,[1*] Wen Cao[1], Yanxin Xie[1], and Carlos Fernandez

J. Zhou, S. Wang, W. Cao, Y. Xie s

[1] School of Information Engineering, Southwest University of Science and Technology, Mianyang 621010, China

[2] School of Electrical Engineering, Sichuan University, Chengdu 610065, China

[3] School of Pharmacy and Life Sciences, Robert Gordon University, Aberdeen AB10-7GJ, UK

Abstract

The accuracy of lithium-ion battery state of charge (SOC) estimation affects the driving distance, battery life, and safety performance of electric vehicles. Herein, the polarization reaction inside the battery is modeled using a second-order fractional-order equivalent circuit model and uses an adaptive genetic algorithm for model parameter identification. Then, an improved adaptive fractional-order backward smoothing square root cubature Kalman filtering algorithm (AFOBS-SRCKF) is proposed by integrating Sage Husa adaptive filtering and backward smoothing processes to optimize the square root cubature Kalman filter for improving the accuracy and adaptability of real-time estimation of SOC in a complex environment. Finally, the algorithm is compared with the integer-order SRCKF, fractional-order SRCKF through simulation, and fractional-order back-ward smoothing SRCKF through simulation. Under complex operating condi-tions, the error sum of SOC estimation of the AFOBS-SRCKF algorithm is controlled within 1.0% and the convergence speed is improved by at least 30%. The results show that the AFOBS-SRCKF algorithm effectively improves the accuracy, stability, and convergence of SOC estimation.

Keywords

adaptive fractional-order backward smoothing square root cubature Kalman filtering; adaptive genetic algorithms; fractional order battery equivalent modeling; lithium-ion batteries; state of charge

Introduction

In recent years, lithium-ion batteries have been greatly developed and widely used as a power source for electric vehicles (EVs) under the concept of sustainable development due to the advantages of high storage capacity, long life, and high output power.[1,2] The battery state of charge (SOC) is one of the core indicators in the battery management system (BMS).[3,4] It can not only provide the remaining power battery charge for the driver to judge the vehicle range, but it can also effectively prevent the battery from being overcharged or overdischarged, thereby protecting the battery and extending its life. As a result, accurate lithium-ion battery charge state estimation has significant research value and significance for improving the driving range and safety performance of EVs.

As an internal SOC, SOC is not directly observed. It can only be estimated by measurable factors such as voltage and current.[5–7] For this reason, domestic and international researchers have proposed several methods for estimating SOC accurately.[8,9] Traditional discharge test methods, ampere-time integration methods, open-circuit voltage methods, and internal resistance methods cannot be estimated in real-time, resulting in large estimation errors. [10,11] Due to the large number of training data samples required, data-driven SOC estimation methods are difficult to implement. As a result, model-based estimation methods are becoming more popular.

The model-based Kalman filter (KF) algorithm approximates system linearization and then optimally estimates system state based on input and output observations.[5,6,12–14] Ge et al.[15] used Taylor's formula to extend the state space equations of the non-linear system by omitting the higher-order terms and proposed an extended KF (EKF) to solve the SOC estimation problem of the nonlinear battery system with an estimation error of no more than 2.5% based on the linear KF algorithm. However, the use of Taylor's formula to extend the nonlinear expressions in higher-order nonlinear battery models can lead to a large number of inaccuracies.[16,17] A traceless Kalman filter (UKF) with a traceless transform (UT) is therefore proposed to replace this process.[18,19] Sakile et al.[20] used the forgetting factor recursive least squares (FFRLS) algorithm to achieve online identification of battery model parameters and ingeniously combined the FFRLS and UKF algorithms for SOC online estimation. However, the UKF algorithm is computationally demanding and the large number of operations leads to a reduction in filtering accuracy when the state dimension of the system exceeds the third order. To reduce

the computational effort and increase the order of the system, the cubature Kalman filtering algorithm (CKF) is proposed using spherical radial cubature criteria.[21] The CKF algo-rithm has higher filtering accuracy and stability than the UKF algorithm.[22] To avoid the influence of filter divergence on system stability, Xing et al.[23] combined the idea of square root filtering with the CKF algorithm and proposed an improved square root cubature Kalman filtering algorithm (SRCKF) to estimate the battery SOC. The maximum error of the estimation result is not more than 3%. Li et al.[24] combined Sage Husa adaptive filtering with the CKF algorithm to achieve adaptive tracking of the battery SOC. However, the filtering efficiency and accuracy of this method are not high enough, and the SOC estimation pro-cess is also susceptible to noise effects easily.

Kalman filtering algorithms are usually based on battery-equivalent circuit models, which can be divided into integer-order models (IOMs) and fractional-order models (FOMs).[25] The IOM is usually used to describe the dynamic characteristics inside the battery and includes the Rint model, the Thevenin model, and the n-order RC model.[26–28] The difficulty of identifying the parameters of IOMs tends to increase with the order of the model, and this can lead to an increase in the mismatch between the parameters and the actual battery state.[29–31] In contrast, the FOMs can describe the activation polarization and concentration polarization phenomena of lithium-ion batteries well.[32–36] The fractional order characteristic of lithium-ion battery is explained through the electrochemical impedance spectrum, and the ideal capacitance of IOM is replaced by constant phase element (CPE) and Warburg impedance to establish FOM with higher accuracy.[32,37–41] Zhu et al.[42] performed SOC estimation by separately combining a FOM and IOM with the adaptive Kalman filter algorithm (AEKF) for SOC estimation, respectively. The experimental results show that combining the AEKF algorithm with the FOM for SOC estimation has higher estimation accuracy and efficiency. Xiao et al.[25] established the fractional-order lithium-ion battery model based on the second-order RC circuit and used the GA algorithm to identify the model parameters. Finally, the fractional order Kalman filter method is used to estimate the battery SOC. The model parameters of this method are not identified with high accuracy, thus resulting in the low accuracy of SOC estimation.

In summary, most researchers have demonstrated that equivalent circuit models for lithium-ion batteries can be constructed based on fractional-order calculus, the SRCKF algorithm can perform SOC of lithium batteries, and Sage Husa adaptive filtering can reduce the effect of noise on SOC estimation. Thus, the combination of methods can lead to better estimation algorithms. In this article, an innovative AFOBS-SRCKF algorithm based on a FOM is proposed for accurate SOC estimation. The primary contributions of this article are as follows. 1) A second-order fractional-order equivalent circuit model for lithium-ion batteries is constructed based on fractional-order calculus theory; 2) An adaptive genetic algorithm (GA) based on model parameter identification is proposed for the optimization problem of model parameter identification; 3) The AFOBS-SRCKF algorithm improves the real-time estimation accuracy of SOC and its adaptive capability in complex environments by introducing Sage Husa adaptive filtering, square root filtering, and backward smoothing process; and 4) The proposed algorithm is compared with the integer order square root cubature Kalman filter (IO-SRCKF) algorithm, fractional-order square root cubature Kalman filter (FO-SRCKF) algorithm, and fractional-order backward smoothing square root cubature Kalman filter (FOBS-SRCKF) algorithm under complex operating conditions. The experimental results show that the AFOBS-SRCKF algorithm has high accuracy, stability, and reliability in performing SOC estimation.

Mathematical Analysis

Second-Order Fractional Order Equivalent Circuit Model

The equivalent circuit model for lithium-ion batteries is based on existing experimental data on the charging and discharging of lithium batteries and is built using electronic components such as voltage sources, resistors, and capacitors to reflect the internal mechanism of the battery. The conventional integer-order equivalent circuit model is unable to accurately describe the capacitive dispersion effect on the surface of the battery electrodes and the particle diffusion phenomenon in the electrodes. Through the electrochemical impedance spectroscopy (EIS) technique, the electrochemical impedance response of the battery can be obtained by exciting the battery with different frequencies of voltage or current, and the results obtained are displayed in the form of Nyquist plots in **Figure 1**a. To accurately model the electrochemical properties of the impedance spectrum, a CPE is introduced instead of the ideal capacitance in the IOM, and a second-order fractional-order equivalent circuit (SO-FOEC) model is proposed. Its structure is shown in Figure 1b.

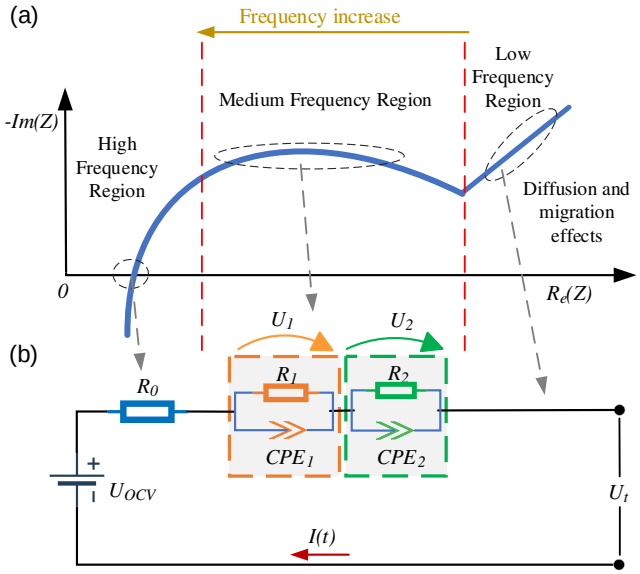

Figure 1. Analysis of FOM: a) Nyquist plot of electrochemical impedance spectrum of lithium battery; b) the structural diagram of the SO-FOEC model.

In the impedance spectrum shown in Figure 1, the high-frequency section intersecting the real axis represents the ohmic resistance R_0 of the lithium-ion battery; the medium-frequency section represents the charge transfer and electric double-layer phenomenon inside the battery, and the low-frequency section corresponds to the diffusion effect of the lithium-ion battery. In the model, U_{OCV} and U_t represent the open-circuit voltage and the terminal voltage of the circuit, respectively, where I correspond to the current flowing through the circuit. CPE represents fractional-order capacitance and its definition of fractional capacitance in the frequency domain is shown in Equation (1).

$$Z_{\mathrm{CPE}} = \frac{1}{Cs^{\alpha}} (0 < \alpha < 1) \tag{1}$$

In Equation (1), Z_{CPE} denotes the complex impedance; C is the fractional order resistance factor of the CPE element; α is the order in the Laplace domain; s is the Laplace operator.

The fractional order calculus uses a Grünwald–Letnikov (G–L) definition, which is defined in the way shown in Equation (2). It enables a direct way of discretizing the fractional-order calculus equation.

$$\begin{cases} D^{\alpha}x(t) = \dfrac{1}{T_S^{\alpha}}\left[x(t) + \displaystyle\sum_{i=1}^{N}(-1)^i \binom{\alpha}{i} x(t-i)\right] \\ \dbinom{\alpha}{i} = \begin{bmatrix} 1, & i = 0 \\ \dfrac{\alpha(\alpha-1)\ \cdots\ [\alpha-(i-1)]}{i!} \end{bmatrix} \end{cases} \tag{2}$$

The loop state equation expression of the second-order fractional-order equivalent circuit model established according to the circuit principle is shown in Equation (3).

$$\begin{cases} D^{\alpha}U_1(t) = -\dfrac{U_1}{R_1\mathrm{CPE}_1} + \dfrac{I(t)}{\mathrm{CPE}_1} \\ D^{\beta}U_2(t) = -\dfrac{U_2}{R_2\mathrm{CPE}_2} + \dfrac{I(t)}{\mathrm{CPE}_2} \\ \mathrm{SOC}(t) = \mathrm{SOC}(t_0) - \dfrac{I(t)T_s}{Q_N} \end{cases} \tag{3}$$

In Equation (2) and (3), α and β are the orders of fractional order capacitance; D^{α} and D^{β} are fractional-order calculus factors.

The observation equation is as follows

$$U_{\mathrm{ocv}}(t) = I(t)R_0 + U_1(t) + U_2(t) + U_{\mathrm{t}}(t) \tag{4}$$

The equivalent circuit is discretized using the fractional inte-gration theory defined by G-L and combined with SOC definition, Equation (5). $[\mathrm{SOC}\ U_1\ U_2]^{\mathrm{T}}$ is selected as the state variable to obtain the discrete state space expression, as shown in Equation (6).

$$\mathrm{SOC}(t) = \mathrm{SOC}(t_0) - \eta \int_0^t \frac{I(t)}{Q_N} \mathrm{d}t \tag{5}$$

$$\begin{cases} \begin{bmatrix} \mathrm{SOC}_{k+1} \\ U_{1,k+1} \\ U_{2,k+1} \end{bmatrix} = \begin{bmatrix} 1 & 0 & 0 \\ 0 & -\dfrac{T_{\mathrm{S}}^{\alpha}}{R_1 R_2} & 0 \\ 0 & 0 & -\dfrac{T_{\mathrm{S}}^{\beta}}{R_1 R_2} \end{bmatrix} \begin{bmatrix} \mathrm{SOC}_k \\ U_{1,k} \\ U_{2,k} \end{bmatrix} + \begin{bmatrix} -\dfrac{T_{\mathrm{S}}}{Q_N} \\ \dfrac{T_{\mathrm{S}}^{\alpha}}{\mathrm{CPE}_1} \\ \dfrac{T_{\mathrm{s}}^{\beta}}{\mathrm{CPE}_2} \end{bmatrix} I_k - \begin{bmatrix} 0 \\ \sum_{i=1}^{N} (-1)^i \binom{\alpha}{i} U_1(k+1-i) \\ \sum_{i=1}^{N} (-1)^i \binom{\beta}{i} U_2(k+1-i) \end{bmatrix} + w_k \\ U_{\mathrm{t},k+1} = U_{\mathrm{ocv}}(\mathrm{SOC}, k+1) - U_1 - U_2 - IR_0 + v_k \end{cases} \tag{6}$$

In Equation (5) and (6), T_S is the sampling time; Q_N is the rated capacity of the battery; w_k is the state noise, and v_k is the mea-surement noise; η is the charging and discharging efficiency of the lithium-ion battery, which is set to 0.98.

Parameter identification based on AGA

The traditional GA for model parameter identification is a random search to obtain the optimal parameters by imitating the biological evolution process. In this article, an improved adaptive genetic algorithm (AGA) is proposed to optimize the traditional GA and solve the problem of fixed values of crossover and variation probabilities in model parameter identification. Compared to traditional GAs, the AGA can adaptively adjust the probability of crossbreeding and mutation for individuals with different degrees of merit, thus selecting the most suitable individuals as parameters for battery model identification and improving the convergence speed, search accuracy, and stability of the GA.

To make the voltage predicted by the SO-FOEC model more accurate, the optimal fitness of the individual designed in this article is determined by finding the minimum value of the absolute value of the terminal voltage error in the group, and the fitness function j(*i*) is shown in Equation (7).

$$J(i) = \sum_{k=1}^{M} [U_{\mathrm{e}}(k) - U_{\mathrm{r}}(k)]^2 \tag{7}$$

In Equation (7), $U_e(k)$ is the predicted output voltage; $U_r(k)$ is the desired output voltage; M is the measured data.

The AGA uses the roulette wheel method to select individuals. The principle is that when the number of random individuals generated is less than the crossover probability, the chromosomes are crossed over using a single-point crossover pairing. The mutation is performed when the number of random individuals generated from the completed crossover chromosomes is less than the mutation probability. Differences between individuals in a population can lead to differences in fitness and genetic probability and the crossover probability P_C and mutation probability P_M for different individuals can be expressed as follows.

$$P_{\mathrm{C}} = \begin{cases} \dfrac{K_1[J_{\max} - J(i)]}{[J_{\max} - J_{\mathrm{ave}}]}, & J \geq J_{\mathrm{ave}} \\ K_2, & J < J_{\mathrm{ave}} \end{cases} \tag{8}$$

$$P_{\mathrm{M}} = \begin{cases} \dfrac{K_3[J_{\max} - J(i)]}{[J_{\max} - J_{\mathrm{ave}}]}, & J \geq J_{\mathrm{ave}} \\ K_4, & J < J_{\mathrm{ave}} \end{cases} \tag{9}$$

In Equation (8) and (9), J_{max} denotes the maximum fitness value in the population; J_{ave} is the average fitness value of the population in each generation; the values of K_1, K_2, K_3, and K_4 range from (0,1) to ensure that the crossover and variation process of different individuals can be adaptively adjusted.

The identification process of the parameters of the SO-FOEC model using the AGA is shown in **Figure 2**.

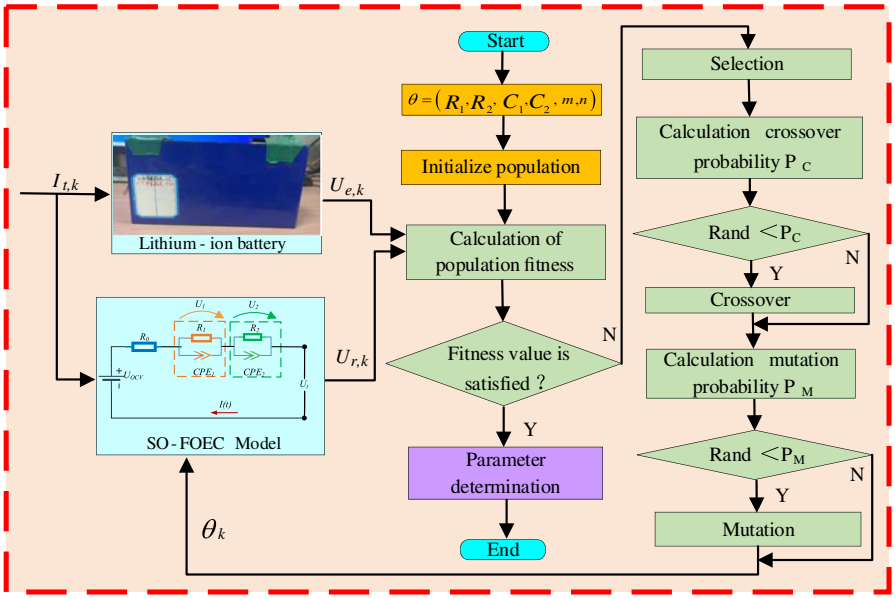

Figure 2. Flow chart for model parameter identification using AGA.

SOC Estimation Based on AFOBS-SRCKF Algorithm

The SRCKF algorithm is based on the fusion of the third-order spherical radial cubature law and the classical Kalman filter system and uses a nonlinear transfer cubature point set to approximate the state posterior distribution in the optimal filtering framework for the nonlinear system. Using the square root matrix instead of the covariance matrix reduces the errors of matrix inversion and decomposition operations in the filtering process and improves the stability of the algorithm.

The idea of the backward smoothing algorithm is to perform backward recursion based on the current and previous sequence of observations and the optimal state estimation sequence obtained by forward filtering to obtain the optimal estimate of the state at any previous moment. Therefore, to improve the filtering accuracy of the nonlinear states, high-precision SOC estimation is achieved. Combining the state space equations established by Equation (10), the second-order fractional order equivalent model, the idea of backward smoothing algorithm, and the SRCKF algorithm are combined to form the fractional order backward smoothing square root cubature Kalman filtering (FOBS-SRCKF) algorithm.

$$\begin{cases} x_{k+1} = f(x_k, u_k) + \omega_k \\ y_{k+1} = h(x_{k+1}, u_{k+1}) + v_{k+1} \end{cases} \tag{10}$$

In Equation (10), x_{k+1} and y_{k+1} are the system state quantity and observation quantity of the system at the moment $k + 1$, respectively; (x_k, u_k) and $h(x_{k+1}$ and $u_{k+1})$ are the nonlinear state transfer function and measurement function, respectively; ω_k and v_{k+1} are the system noise.

The FOBS-SRCKF algorithm includes two forward filtering operations and one backward smoothing operation. The basic block diagram of the FOBS-SRCKF algorithm operation is shown in **Figure 3** below. In this algorithm, the first forward filtering can remove some errors produced during operation, and the second forward filtering performed after the backward smoothing process can further eliminate the errors, thus improving the filtering numerical accuracy of the algorithm and therefore improving the real-time estimation accuracy of SOC. The following are the precise steps to estimate SOC.

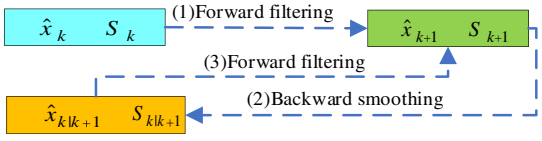

Figure 3. Basic block diagram of FOBS-SRCKF algorithm operation. 1) Forward filtering; 2) Backward smoothing; 3) Forward filtering.

Step	Content
①	Initialization of Parameters

1.1. Initialize system noise covariance Q_0 and measurement noise covariance R_0.

1.2. Initialized state estimates x_0 and covariance P_0.

$$\begin{cases} x_0 = E(x_0) \\ P_0 = E\left[(\hat{X}_0 - X_0)(\hat{X}_0 - X_0)^{\mathrm{T}}\right] \end{cases} \tag{11}$$

② Time update

2.1. Decomposition of covariance P_0 using Cholesky.

$$S_0 = \mathrm{chol}(P_0) \tag{12}$$

2.2. Calculation of cubature points $X_{j,k|k}$.

$$X_{j,k|k} = S_{k|k}\xi_j + \hat{x}_{k|k} \tag{13}$$

In Equation (14), $S_{k|k}$ is the square root of the state error covariance P at moment k; ξ_j is the set of cubature points with the following expressions for its n-dimensional state quantities.

$$\xi_j = \begin{cases} \sqrt{n}[E]_j & j = 1, 2, \ldots, n \\ -\sqrt{n}[E]_j & j = n+1, n+2 \ldots, 2n \end{cases} \tag{14}$$

2.3. Propagation of cubature points through state equations and prediction of system state quantities.

$$\begin{cases} X^*_{j,k+1|k} = f\left(X_{j,k|k}, u_k\right), \quad j = 1, 2, \ldots, n \\ \overline{x}_{k+1|k} = \dfrac{1}{2n}\displaystyle\sum_{j=1}^{2n} X^*_{j,k+1|k} \end{cases} \tag{15}$$

2.4. Calculate the square root of the state error covariance prediction $\overline{S}_{k+1|k}$.

$$\begin{cases} \overline{S}_{k+1|k} = Tria\left(\lambda^*_{k+1|k}, S_Q\right) \\ \lambda^*_{k+1|k} = \dfrac{1}{\sqrt{2n}}\displaystyle\sum_{j=1}^{2n}\left(X^*_{j,k+1|k} - \overline{x}_{k+1|k}\right) \\ S_Q = \mathrm{chol}(Q_k) \end{cases} \tag{16}$$

③ Measurement update

3.1. Update cubature points.

$$X^*_{j,k+1|k} = \overline{S}_{k+1|k}\xi_j + \overline{x}_{k+1|k}, \quad j = 1, 2, \ldots, n \tag{17}$$

3.2. Propagate cubature points through measurement equations and calculate measurement predictions.

$$\begin{cases} Y_{j,k+1|k} = h\left(X_{j,k+1|k}, u_{k+1}\right) \\ \overline{y}_{k+1|k} = \dfrac{1}{2n}\displaystyle\sum_{j=1}^{2n} Y_{j,k+1|k} \end{cases} \tag{18}$$

3.3. Calculate the square root of the innovation covariance matrix $S^z_{k+1|k}$ and the square root of the mutual covariance $P^z_{k+1|k}$.

$$\begin{cases} S^z_{k+1|k=}\mathrm{Tria}\left(\gamma_{k+1|k}, S_R\right) \\ P^z_{k+1|k=}\chi_{k+1}\gamma_{k+1} \\ S_R = \mathrm{chol}(R_k) \\ \chi_{k+1|k} = \dfrac{1}{\sqrt{2n}}\displaystyle\sum_{j=1}^{2n}\left(X_{j,k+1|k} - \overline{x}_{k+1|k}\right) \\ \gamma_{k+1|k} = \dfrac{1}{\sqrt{2n}}\displaystyle\sum_{j=1}^{2n}\left(Y_{j,k+1|k} - \overline{y}_{k+1|k}\right) \end{cases} \tag{19}$$

Step	Content

3.4. Calculate Kalman gain K_{k+1}; system state cubature estimate $\hat{x}_{k+1|k+1}$; the square root of state error covariance $S_{k+1|k+1}$.

$$\begin{cases} K_{k+1} = \left(P^z_{k+1|k} \Big/ S^z_{k+1|k}{}^{\mathrm{T}}\right) \Big/ S^z_{k+1|k} \\ \hat{x}_{k+1|k+1} = \overline{x}_{k+1|k} + K_{k+1}\left(Y_{k+1} - \hat{y}_{k+1|k}\right) \\ S_{k+1|k+1} = \mathrm{Tria}\left[\chi_{k+1|k} - K_{k+1}\gamma_{k+1|k}, K_{k+1}S_R\right] \end{cases} \tag{20}$$

④ Backward smoothing estimation

4.1. Obtain state smoothing valuation and backward smoothing gain.

$$\begin{cases} \hat{x}_{k|k+1} = \hat{x}_k + W_k\left(\hat{x}_{k+1|k+1} - \hat{x}_{k+1|k}\right) \\ W_k = \left(P^z_{k+1} \Big/ S^{\mathrm{T}}_{k+1|k}\right) \Big/ S^{\mathrm{T}}_{k+1|k} \end{cases} \tag{21}$$

4.2. Obtain the square root value of the smoothing estimation error covariance matrix.

$$S_{k+1|k} = \mathrm{Tria}\left[\chi_{k+1} - W_k\chi^*_{k+1}, W_kS_Q, W_kS_{k+1}\right] \tag{22}$$

⑤ The backward smoothed value is used as the initial value at the moment k + 1 to perform forward filtering again according to steps ② and ③ to obtain the state estimate at the next moment and perform the iterative calculation to estimate the SOC value.

When the FOBS-SRCKF algorithm is accompanied by complex changes in the external environment, the process noise and measurement noise, which are regarded as constant values during the iterative process, will be subject to systematic random perturbations. This will cause the noise value to change and the accuracy of the algorithm to decrease. Thus, this article introduces the Sage Husa adaptive filtering algorithm. Based on the Sage Husa maximum, a posteriori estimator, and the sequence of output voltage residuals from the battery model, the two noise covariance matrices are adaptively updated to Equation (23).

$$\begin{cases} \hat{q}_{k+1} = (1 - d_{k+1})\hat{q}_k + d_{k+1}\left[\hat{x}_{k+1} - \sum_{j=1}^{2n+1} \omega_j f\left(X_{j,k+1}, u_{k+1}\right)\right] \\ \hat{r}_{k+1} = (1 - d_{k+1})\hat{r}_k + d_{k+1}\left[\hat{y}_{k+1} - \sum_{j=1}^{2n+1} \omega_j h\left(X_{j,k+1}, u_{k+1}\right)\right] \\ \hat{Q}_{k+1} = (1 - d_{k+1})\hat{Q}_{k+}d_{k+1}\left[K\varepsilon_{k+1}\varepsilon^{\mathrm{T}}_{k+1}K^{\mathrm{T}}\right] \\ \hat{R}_{k+1} = (1 - d_{k+1})\hat{R}_{k+}d_{k+1}\left[\varepsilon_{k+1}\varepsilon^{\mathrm{T}}_{k+1}\right] \\ \varepsilon_{k+1} = \hat{y}_{k+1} - Y_{k+1} \end{cases} \tag{23}$$

In Equation (23), $d_{k+1} = (1 - b)/\left(1 - b^{k+1}\right)$, b is the forgetting factor, usually in the range of 0.950–0.998, and the value of 0.986 in this study; q_{k+1}, r_{k+1}, Q_{k+1}, R_{k+1} are the process noise, mea-surement noise, process noise covariance, and measurement noise covariance; ε_{k+1} is the output residual series.

The block diagram of the adaptive fractional-order backward smoothing square root cubature Kalman filter (AFOBS-SRCKF) algorithm for accurately estimating the SOC is shown in Figure 4.

Analysis

Experimental Test Platform

To verify the accuracy of parameter identification of the second-order fractional order equivalent circuit model proposed in this article and the accuracy of the AFOBS-SRCKF algorithm for estimating SOC, an experimental platform was constructed using a BTS200-100-104 battery testing device and temperature control equipment, as shown in Figure 5.

In the experiment, a lithium-ion battery with a rated capacity of 70 Ah is selected as the research object. The lithium-ion battery is placed in a temperature controller and the experimental operating environment temperature is set at 25 °C to reduce the influence of temperature on the operating condition of the lithium-ion battery. Experimental verification is carried out on the experimental platform under three operating conditions: hybrid pulse power characteristics (HPPC), Beijing bus dynamic stress test (BBDST), and dynamic stress test (DST).

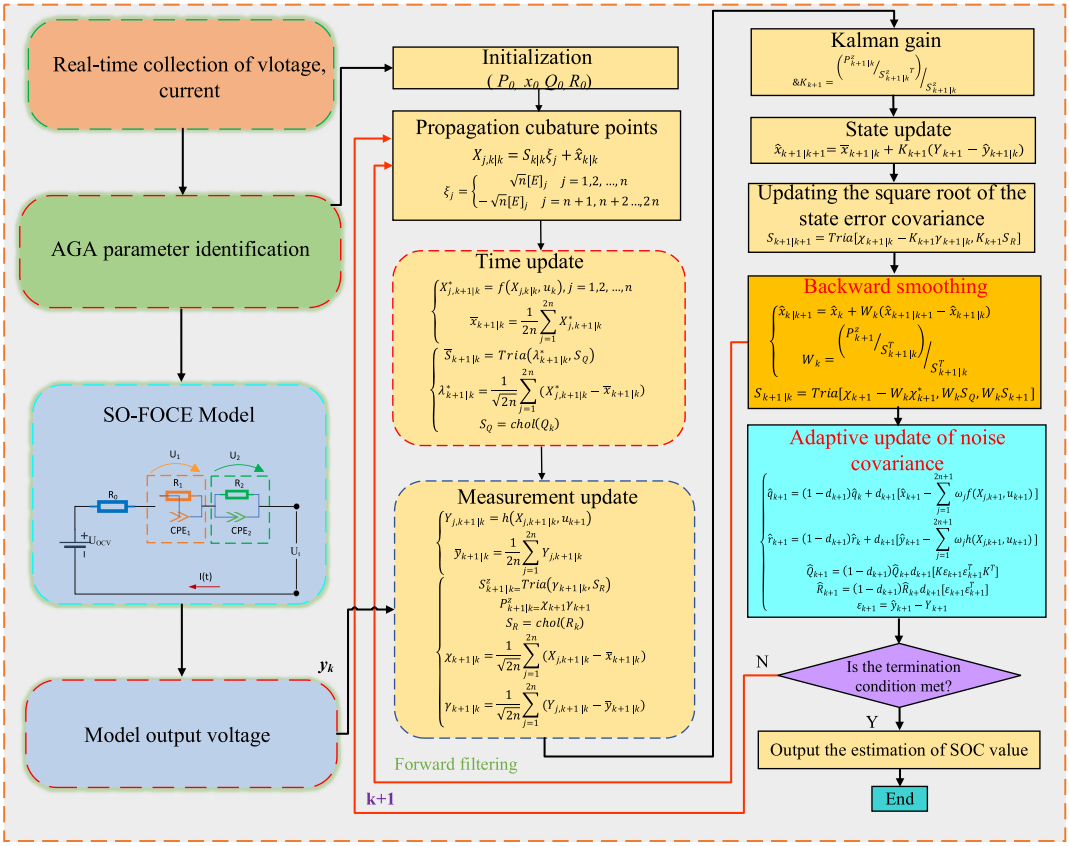

Figure 4. Flowchart of the AFOBS SRCKF algorithm for SOC estimation.

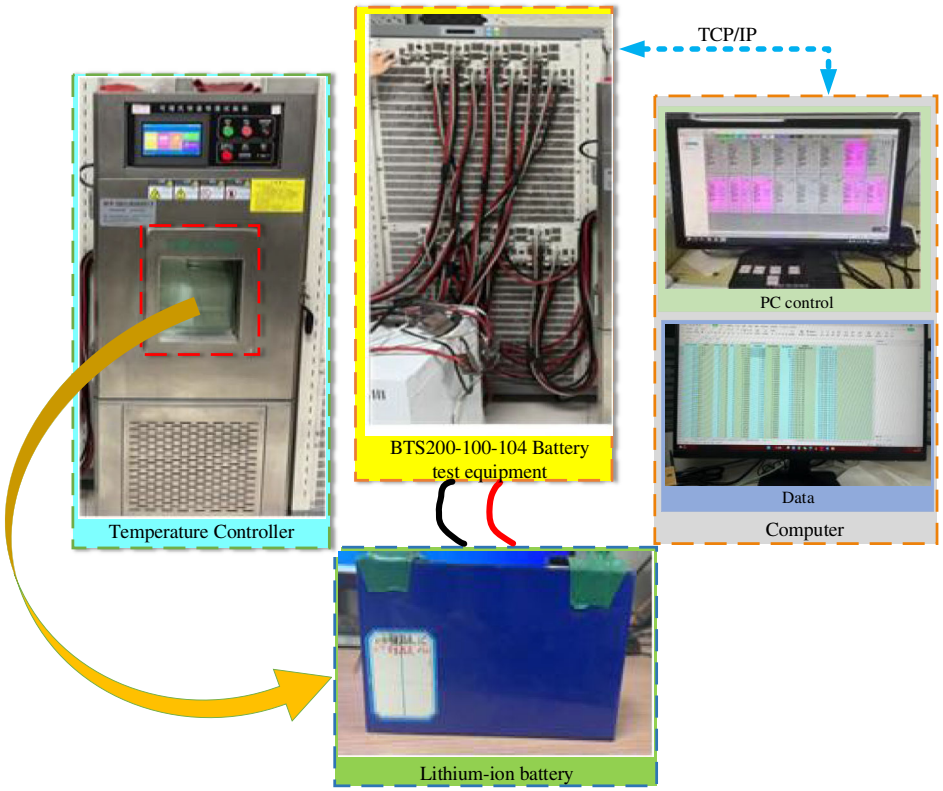

Figure 5. Experimental test platform.

Parameter Identification and Accuracy Verification of the Model

The lithium-ion battery is cyclically charged and discharged in the experimental environment at a room temperature of 25 °C. The battery is charged at 1 C times constant current to the upper termination voltage of 4.2 V and then charged at a constant voltage. After charging is completed, the battery is set aside for 2 h to stabilize the battery voltage. Then the lithium-ion battery at a constant current rate of 1 C with a discharge cutoff voltage of 2.75 V is discharged. Discharge is stopped each time the discharge point reaches the SOC sampling point, and the battery is placed for 30 min and continues to discharge until the battery SOC is 0, ending the experiment. One of the pulse processes is shown in **Figure 6**.

At the moment of charging or power-off of fractional-order equivalent battery model, the voltage of resistance R_0 terminal will change instantaneously. Therefore, the linear parameter resistance R_0 can be obtained by Equation (24). The remaining nonlinear parameters R_1, R_2, C_1, C_2, α and β in the model are searched for the global optimal solution by the AGA algorithm.

$$R_0 = \frac{[(U_a - U_b) + (U_d - U_c)]}{2I} \tag{24}$$

Under HPPC working conditions, the parameters of the second-order fractional order equivalent (SO-FOEC) model and second-order integer order equivalent (SO-IOEC) model are identified using the AGA. Meanwhile, the parameter identification of the SO-IOEC model is performed using GA. All the identification results are shown in **Table 1**.

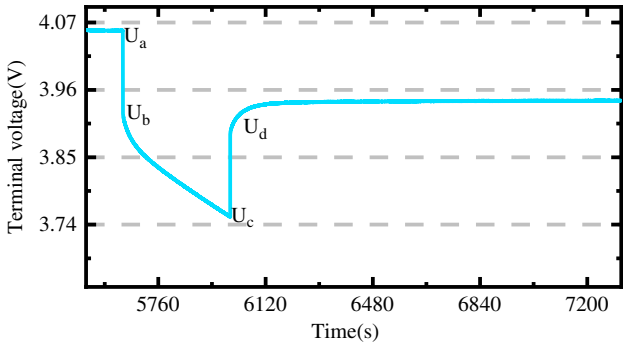

Figure 6. Schematic diagram of a pulse process.

Table 1. Model parameter identification results based on different algorithms.

Algorithm	Model type	R_0 [mΩ]	R_1 [mΩ]	R_2 [mΩ]	C_1 [F]	C_2 [F]	α	β
AGA	SO-FOEC	2.50	0.170	0.200	51 430	64 484	0.9819	0.9958
	SO-IOEC	2.50	0.160	0.210	68 914	82 458	/	/
GA	SO-IOEC	2.48	0.157	0.221	70 521	83 434	/	/

As shown in Table 1, the results for the resistance are essentially the same. Since the dynamic characteristics of the battery throughout the discharge process are expressed by the capacitance, the main difference lies in the polarization capacitance C_1 and the concentrated polarization capacitance C_2.

To verify the superiority of the proposed AGA parameter iden-tification and the accuracy of the SO-FOEC model, these data are input to the equivalent model of the battery that utilizes the AGA and GA for parameter identification, respectively, to obtain the real-time terminal voltages of the battery model. End voltage simulation results are compared with the actual measurement results, as shown in **Figure 7**.

Figure 7a shows the voltage comparison results of different models. U_Real is the actual measured voltage. U_SO-FOEC -(AGA) is the simulated voltage value estimated based on the second-order FOM of AGA. U_SO-IOEC - (AGA) is the simulated voltage value estimated based on the second-order IOM of AGA. U_SO-IOEC - (GA) is the simulated voltage value estimated based on the second-order integer order model of GA. As can be seen from the enlarged figure display, the SO-FOEC model estimate based on AGA is closest to the actual measured voltage. In Figure 7b, it can be concluded from the voltage simulation error curve scores that the maximum error and root mean square error of the SO-IOEC model based on AGA are 1.36% and 1.10%, while the maximum error and root mean square error of the SO-IOEC model based on GA are 1.43% and 1.29%. The comparison reveals that the parameter identification accuracy of AGA is higher than that of GA. The maximum error and root mean square error of the SO-FOEC model based on AGA are divided into 1.31% and 1.06%. Comparison with the SO-IOEC model based on AGA reveals that the identification results of the SO-FOEC model proposed in this article have less error and the results are better than those of the SO-IOEC model for the subsequent battery SOC.

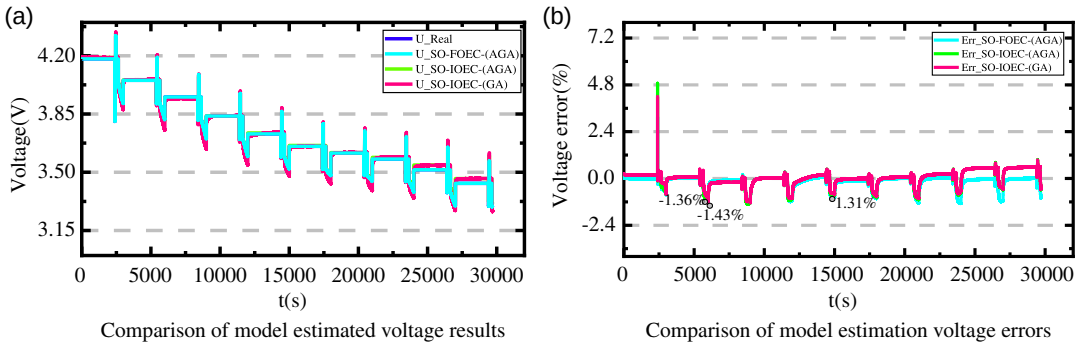

Figure 7. Comparison results in HPPC working conditions. a) Comparison of model estimated voltage results. b) Comparison of model estimation voltage errors.

Analysis of SOC Estimation Results under Complex Operating Conditions

To verify the feasibility, accuracy, and convergence of the algorithm proposed in this article in a complex practical application environment. The initial SOC error is set to 20%, and the experimental value of SOC at each time point is calculated by the ampere–time integration method with the known initial value of SOC. To make the AFOBS-SRCKF algorithm better simulate the battery operation condition with the IO-SRCKF algorithm, FO-SRCKF algorithm, and FOBS-SRCKF algorithm, the comparison and validation of different algorithms were chosen under the conditions of HPPC operating conditions. The experimental results are shown in **Figure 8**.

As shown in Figure 8a, the overall SOC estimation results of the IO-SRCKF and FO-SRCKF algorithms fluctuate greatly, while the AFOBS-SRCKF algorithm and the FOBS-SRCKF algorithm track the true SOC values well throughout the estimation process. Among them, the predicted value AFOBS-SRCKF algorithm is closer to the real values and the estimation results are significantly better than the remaining three algorithms. From the enlarged figure, it can be seen that the AFOBS-SRCKF algorithm can converge to the true value faster than the other three algorithms, and the convergence is better than the remaining three algorithms. Figure 8b shows the errors of these four algorithms in estimating the SOC. Among them, the error of the AFOBS-SRCKF algorithm is controlled within 0.5%. Compared with the remaining three algorithms, the error is significantly smaller. It not only effectively reduces the influence of noise, but also improves the estimation accuracy. This fully illustrates the accuracy and effectiveness of the algorithm proposed in this article in estimating SOC.

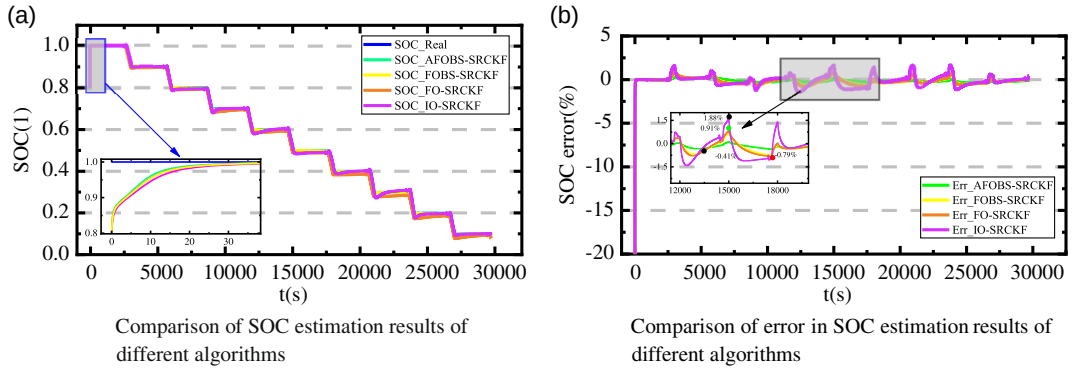

Figure 8. SOC estimation results and errors under HPPC working conditions. when SOC initial is 0.8. a) Comparison of SOC estimation results of different algorithms. b) Comparison of error in SOC estimation results of different algorithms.

The analysis in **Table 2** shows that the maximum estimation error of the AFOBS-SRCKF algorithm is 0.41%, the RMSE is 0.38%, and the convergence speed is 28 s. Compared with the FOBS-SRCKF algorithm, the maximum estimation error is reduced by 48.1% and the RMSE is reduced by 43.3%. It indicates that adding Sage Husa adaptive filtering can effectively reduce the effect of noise on estimation accuracy. Compared with the FO-SRCKF algorithm, the maximum estimation error of the FOBS-SRCKF algorithm is reduced by 13.2%, the RMSE is reduced by 20.3%, and the convergence speed is increased by 10.8%. It indicates that the idea of adding the backward smoothing algorithm effectively improves the estimation of SOC efficiency and accuracy. The FO-SRCKF algorithm has less error and higher estimation accuracy than the IO-SRCKF algorithm for estimating SOC. The combined analysis of Figure 8 and Table 2 concludes that the AFOBS-SRCKF algorithm can track and estimate the SOC of lithium-ion batteries more accurately than the other three algorithms.

Table 2. Error analysis under HPPC operating conditions.

Method	Initial value	HPPC		
		Convergence time [s]	Maximum error [%]	RMSE [%]
AFOBS-SRCKF	0.8	28	0.41	0.38
FOBS-SRCKF	0.8	33	0.79	0.67
FO-SRCKF	0.8	37	0.91	0.84
IO-SRCKF	0.8	41	1.88	1.69

To better simulate the complex working conditions of the actual driving of EVs, the experiments are selected under DST working conditions and BBDST working conditions to verify the feasibility and accuracy of the proposed algorithm for SOC estimation. The experimental results of SOC estimation of the AFOBS-SRCKF algorithm with IO-SRCKF algorithm, FO-SRCKF algorithm, and FOBS-SRCKF algorithm by setting the initial value of SOC with an error of 20% are shown in **Figure 9** and **10**. **Table 3** and **4** show the analysis and comparison results of different algorithms under different operating conditions.

From Figure 9a, it can be seen that the curve fit of the AFOBS-SRCKF algorithm is closest to the reference value under the DST operating conditions, and it converges quickly and fits well compared to the other three algorithms. Then, by comparing the curves of the FO-SRCKF algorithm and the IO-SRCKF algorithm, it can be seen that the FO-SRCKF algorithm based on the fractional-order model has better estimation, indicating that the fractional-order model also indirectly improves the estimation accuracy of the SOC. From Figure 9b, it can be seen that the estimation error of SOC at the end of discharge is relatively large due to the serious electrochemical reaction inside the battery. The error of the AFOBS-SRCKF algorithm is controlled within 0.81%, which reflects the estimation accuracy of the algorithm for SOC of lithium-ion batteries.

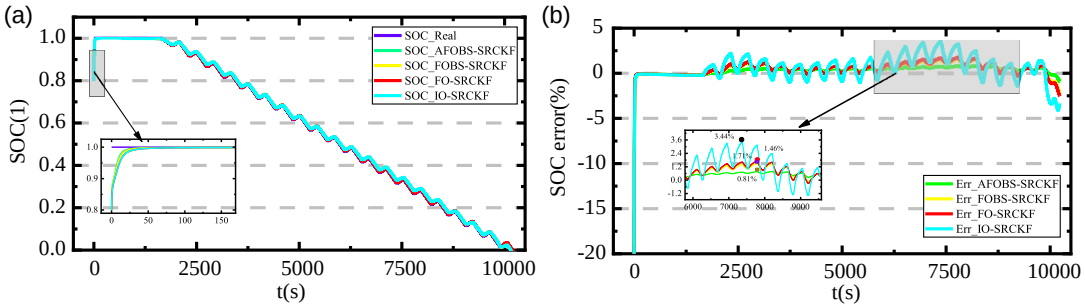

Comparison of SOC estimation results of different algorithms

Comparison of error in SOC estimation results of different algorithms

Figure 9. SOC estimation results and errors under DST working conditions when SOC initial is 0.8. a) Comparison of SOC estimation results of different algorithms. b) Comparison of error in SOC estimation results of different algorithms.

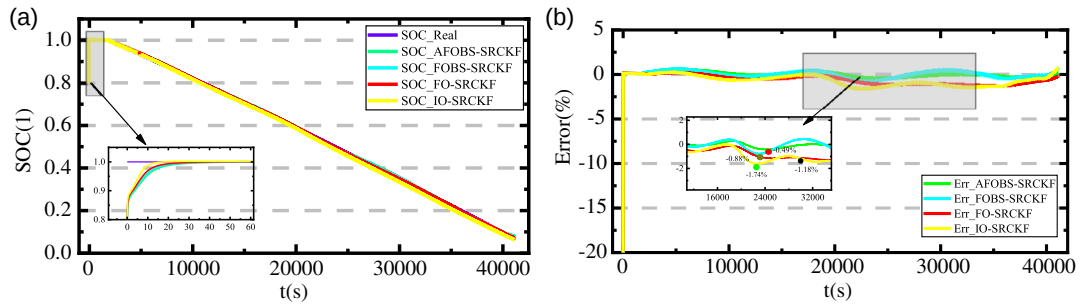

Comparison of SOC estimation results of different algorithms

Comparison of error in SOC estimation results of different algorithms

Figure 10. SOC estimation results and errors under BBDST working conditions when SOC initial is 0.8. a) Comparison of SOC estimation results of different algorithms. b) Comparison of error in SOC estimation results of different algorithms.

Table 3. Error analysis under DST operating conditions.

Method	Initial value	DST		
		Convergence time [s]	Maximum error [%]	RMSE [%]
AFOBS-SRCKF	0.8	38	0.81	0.68
FOBS-SRCKF	0.8	50	1.46	1.31
FO-SRCKF	0.8	69	1.71	1.57
IO-SRCKF	0.8	80	3.44	3.25

Table 4. Error analysis under BBDST operating conditions.

Method	Initial value	BBDST		
		Convergence time [s]	Maximum error [%]	RMSE [%]
AFOBS-SRCKF	0.8	23	0.49	0.35
FOBS-SRCKF	0.8	28	0.88	0.74
FO-SRCKF	0.8	34	1.18	0.99
IO-SRCKF	0.8	40	1.74	1.56

Based on the further analysis in Table 3, it can be concluded that the maximum error and RMSE of the AFOBS-SRCKF algorithm are 0.81% and 0.68%, respectively, with a convergence time of 38 s. Compared with the FOBS-SRCKF algorithm, the error of the AFOBS-SRCKF algorithm is reduced by at least 48.1%. It indicates that the addition of Sage Husa adaptive filtering can improve SOC estimation accuracy. The FOBS-SRCKF algorithm converges 27.5% faster than the FO-SRCKF algorithm, and the estimation performance is better, indicating that the optimization effect of backward smoothing is obvious. Among them, compared with the IO-SRCKF algorithm, the maximum error and RMSE of the FO-SRCKF algorithm are reduced by 50.2%and 51.6%, respectively, and the convergence speed is improved by 13.8%. This indicates that the FOM reduces the error of SOC estimation to a certain extent and improves the accuracy and stability of SOC estimation.

As shown in Figure 10a, the overall estimation of SOC under the BBDST operating conditions shows a convergence trend of decreasing fluctuation. Among them, the SOC curve of the AFOBS-SRCKF algorithm almost coincides with the true value curve, indicating that its tracking performance is better than the other three algorithms. From Figure 10b, it can be seen that the AFOBS-SRCKF algorithm has a smaller error, faster convergence, and higher stability than the other three algorithms, and the advantages are more obvious. Compared with the IO-SRCKF algorithm, the error and fluctuation range of the FO-SRCKF algorithm are smaller, indicating that the proposed fractional-order battery model algorithm indirectly improves the accuracy of SOC estimation.

As shown in Table 4, the AFOBS-SRCKF algorithm estimated the SOC with a maximum error of 0.49% and an RMSE of 0.35%. Compared with the FOBS-SRCKF algorithm, the maximum estimation error of the AFOBS-SRCKF algorithm is reduced by 31.3% and the RMSE is reduced by 52.7%. It indicates that the inclusion of Sage Husa adaptive filtering can reduce the SOC estimation error. Compared with the FO-SRCKF algorithm, the error of the FOBS-SRCKF algorithm is reduced by at least 25.2% and the convergence speed is increased by 17.6%. In particular, the SOC estimation error of the FO-SRCKF algorithm is reduced by at least 36.2% compared to the IO-SRCKF algorithm. This indicates that the FOM improves the accuracy of SOC estimation to some extent. Combined with the convergence time and error, it shows that the AFOBS-SRCKF algorithm has high estimation accuracy and its convergence and filtering effect is very good.

Conclusion

Accurate SOC estimation is crucial for BMS to extend the range, battery life, and safety performance of EVs. In this article, an innovative AFOBS-SRCKF algorithm based on a FOM is proposed for SOC estimation. Through validation and comparative analysis under complex operating conditions, the following conclusions are drawn: 1) Under HPPC working conditions, the parameter identification error of the AGA based on the SO-FOEC circuit model is controlled to within 1.31%, which is 3.61% lower than that of the SO-IOEC model. By comparing the results of parameter identification under the same model, it is found that the parameter identification error of the AGA model is 14.7% lower than the GA identification error; and 2) The AFOBS-SRCKF algorithm, under complex operating conditions, controls the maximum error and RMSE of SOC estimation within 1.0% and 0.8%, respectively, and improves the convergence speed by at least 30% or more, The algorithm outperforms the IO-SRCKF algorithm, the FO-SRCKF algorithm, and the FOBS-SRCKF algorithm in terms of estimation accuracy and convergence speed.

In conclusion, the study completely demonstrates the AFOBS-SRCKF algorithm's effectiveness and superiority in SOC estimation. This study provides the theoretical foundation for battery performance and condition monitoring, ensuring drivers can safely operate EVs. However, temperatures during actual driving are complicated and varied, and future research will focus on the impact of real-time temperature variations on battery SOC calculation.

Acknowledgements

This work was supported by the National Natural Science Foundation of China (no. 62173281), Sichuan Provincial Science and Technology Program (no. 23ZDYF0734NSFSC4444), Dazhou City School Partnership Program (no. DZXQHZ006), Technology Pole Talent Summit Program (no. KJCRCFH08), and Robert Gordon University.

Conflict of Interest

The authors declare no conflict of interest.

Data Availability Statement

The data that support the findings of this study are available from the corresponding author upon reasonable request.

References

[1] H. Wei, Y. Zhong, L. Fan, Q. Ai, W. Zhao, R. Jing, Y. Zhang, *J. Power Sources* **2021**. *513*, 230531
[2] K. Xie, L. Han, K. Ma, F. Wang, B. Wang, J. Chen, Y. Gao, *Energy Rep.* **2022**, *8*, 639.
[3] K. W. E. Cheng, B. P. Divakar, H. Wu, K. Ding, H. F. Ho, *IEEE Trans. Veh. Technol.* **2011**, *60*, 76.
[4] M. S. Ramkumar, C. S. R. Reddy, A. Ramakrishnan, K. Raja, S. Pushpa, S. Jose, M. Jayakumar, S. J. S. Chelladurai, *Adv. Mater. Sci. Eng.* **2022**, *2022*, 3379574.
[5] M. Adaikkappan, N. Sathiyamoorthy, *Int. J. Energy Res.* **2022**, *46*, 2141.
[6] N. Bhushan, S. Mekhilef, K. S. Tey, M. Shaaban, M. Seyedmahmoudian, A. Stojcevski, *Sustainability* **2022**, *14*, 15912.
[7] Z. Cui, L. Wang, Q. Li, K. Wang, *Int. J. Energy Res.* **2022**, *46*, 5423.
[8] P. Shrivastava, P. A. Naidu, S. Sharma, B. K. Panigrahi, A. Garg, J. *Energy Storage* **2023**, *64*, 107159
[9] M. Ul Hassan, S. Saha, M. E. Haque, S. Islam, A. Mahmud, N. Mendis, *Sustainable Energy Technol. Assess.* **2022**. *54*, 102801.
[10] P. Pillai, S. Sundaresan, P. Kumar, K. R. Pattipati, B. Balasingam, *Energies* **2022**, *15*, 6803.
[11] L. Yun, B. Panda, L. Gao, A. Garg, X. Meijuan, D. Chen, C.-T. Wang, *Math. Probl. Eng.* **2018**, *2018*, 8165164.
[12] M. Kwak, B. Lkhagvasuren, H. S. Jin, G. Seo, S. Bong, J. Lee, *Int. J. Electrochem. Sci.* **2022**, *17*, 220218.
[13] B. Yang, G. Li, W. Tang, H. Li, *Front. Energy Res.* **2022**, *10*, https://doi. org/10.3389/fenrg.2022.1027439.
[14] W. Zhou, Y. Zheng, Z. Pan, Q. Lu, *Processes* **2021**, *9*, 1685.
[15] C. Ge, Y. Zheng, Y. Yu, *J. Energy Storage* **2022**, *55*, 105474.
[16] C. Qi, S. Wang, W. Cao, P. Yu, Y. Xie, *Int. J. Circuit Theory Appl.* **2022**. *50*, 3487.
[17] J. Xing, P. Wu, *Sustainability* **2021**, *13*, 5046.
[18] J. Guo, S. Liu, R. Zhu, *Front. Energy Res.* **2023**, *10*, https://doi.org/10. 3389/fenrg.2022.998002.
[19] M. Hossain, M. E. Haque, M. T. Arif, *J. Energy Storage* **2022**, *51*, 104174.
[20] R. Sakile, U. K. Sinha, *Adv. Theor. Simul.* **2022**, *5*, 2100397.
[21] J. He, S. Meng, F. Yan, *Front. Energy Res.* **2022**, *10*, https://doi.org/10. 3389/fenrg.2022.914291.
[22] S. Zhuang, Y. Gao, A. Chen, T. Ma, Y. Cai, M. Liu, Y. Ke, *J. Electrochem. Soc.* **2022**, *169*, 100521.
[23] X. Shu, G. Li, Y. Zhang, S. Shen, Z. Chen, Y. Liu, *IEEE Trans. Transp. Electrif.* **2021**, *7*, 1271.
[24] X. Li, Z. Huang, J. Tian, Y. Tian, *Energy* **2021**, *220*, 119767.
[25] R. Xiao, J. Shen, X. Li, W. Yan, E. Pan, Z. Chen, *Energies* **2016**, *9*, 184
[26] D. Salazar, M. Garcia, *Energies* **2022**, *15*, 7204.
[27] L. Zhang, S. Wang, D.-I. Stroe, C. Zou, C. Fernandez, C. Yu, *Energies* **2020**, *13*, 2057.
[28] X. Zhou, Y. Liu, P. Chang, F. Xue, T. Zhang, *Electronics* **2022**, *11*, 1758.
[29] G. Barletta, P. Diprima, D. Papurello, *Energies* **2022**, *15*, 6207.
[30] H. Fatoorehchi, M. Ehrhardt, *J. Energy Storage* **2022**, *45*, 103746.
[31] Z. Lyu, R. Gao, *Int. J. Energy Res.* **2020**, *44*, 10262.
[32] S. Liu, X. Dong, Y. Zhang, *IEEE Access* **2019**, *7*, 122949.
[33] P. Rodríguez-Iturriaga, J. Alonso-del-Valle, S. Rodríguez-Bolívar, D. Anseán, J. C. Viera, J. A. López-Villanueva, *J. Energy Storage* **2022**, *56*, 105810.
[34] O. O. Solomon, W. Zheng, J. Chen, Z. Qiao, *J. Energy Storage* **2022**, *49*, 104007.
[35] J. Tian, R. Xiong, W. Shen, F. Sun, *Sci. China Technol. Sci.* **2020**, *63*, 2211.
[36] L. Xing, X. Wu, L. Ling, L. Lu, L. Qi, *Appl. Sci.* **2022**, *12*, 9524.
[37] L. He, Y. Wang, Y. Wei, M. Wang, X. Hu, Q. Shi, *Energy* **2022**, *244*, 122627.
[38] M. He, S. Wang, C. Fernandez, C. Yu, X. Li, E. D. Bobobee, *Int. J. Electrochem. Sci.* **2021**, *16*, 21054.
[39] L. Ling, Y. Wei, *IEEE Access* **2021**, *9*, 47588.
[40] N. Ma, H. Yin, K. Wang, *Energies* **2023**, *16*, 5240.
[41] M. Zhang, Y. Liu, D. Li, X. Cui, L. Wang, L. Li, K. Wang, *Energies* **2023**, *16*, 1599.
[42] Q. Zhu, M. Xu, W. Liu, M. Zheng, *Energy* **2019**, *187*, 115880.